doi: 10.82124/CEAS-GNC-2026-063 CEAS-GNC-2026-063

Hardware in the Loop Experimental Validation of a Path Controller for Airborne Wind Energy Systems

Jorge González-García Department of Aerospace Engineering, Universidad Carlos III de Madrid, Avenida de la Universidad 30, 28911 Leganés (Madrid), Spain. jorgegga@ing.uc3m.es

Francisco DeLosRíos-Navarrete Department of Aerospace Engineering, Universidad Carlos III de Madrid, Avenida de la Universidad 30, 28911 Leganés (Madrid), Spain.
CT Ingenieros A.A.I. S.L. Avenida Leonardo Da Vinci 22, 28050 Getafe (Madrid), Spain francisco.delosrios@ctingenieros.es

David Santos-Martín Department of Electrical Engineering, Universidad Carlos III de Madrid, Avenida de la Universidad 30, 28911 Leganés (Madrid), Spain. dsmartin@ing.uc3m.es

Gonzalo Sánchez-Arriaga Department of Aerospace Engineering, Universidad Carlos III de Madrid, Avenida de la Universidad 30, 28911 Leganés (Madrid), Spain. gonsanch@ing.uc3m.es

ABSTRACT

Airborne Wind Energy (AWE) systems require reliable control architectures to achieve autonomous and repeatable flight under realistic operating conditions. To support controller development while reducing the cost and risk associated with field experiments, a Hardware-in-the-Loop (HIL) platform for closed-loop validation of external flight controllers is presented. The proposed setup combines a high-fidelity kite dynamics model executed in real time, with a Ground Control Unit (GCU), wireless communication modules, and physical actuators. The platform is assessed in terms of computational performance, communication latency, and path-following capability. The results show that the proposed HIL setup sustains real-time operation and enables stable closed-loop tracking of ten figure-eight trajectories, providing a practical intermediate validation stage between offline simulation and flight testing.

Keywords: Airborne Wind Energy, Hardware in the loop, Real-time, Control

1 Introduction

Airborne Wind Energy (AWE) systems use tethered aircraft to harvest wind energy at altitudes that are typically beyond the operating range of conventional wind turbines [1]. In these systems, the airborne platform can be a kite or a fixed-wing aircraft [2], and the performance depends strongly on the capability to fly efficient trajectories under changing wind and operating conditions [3]. For this reason, experimental validation is a necessary step in the development of AWE technology. Several works have reported flight tests with experimental ground stations and autonomous controllers [4–7]. However, flight testing is costly, weather-dependent, and subject to safety and logistical constraints. These factors limit the number of test campaigns and slow down the iteration between controller design, implementation, and validation.

Hardware-in-the-loop (HIL) techniques can be used as an intermediate step between offline simulation and field experiments [8]. In AWE, previous HIL and emulator-based works have mainly focused on

specific subsystems, especially ground-generation emulation and power-stage validation [8–11]. By contrast, fewer works have addressed closed-loop validation environments for guidance and control in which the real controller hardware is coupled with a high fidelity dynamic kite model. The value of such an environment depends on two aspects: the fidelity of the plant model and its capability to run in real time. Quasi-static models [12] are computationally efficient and useful for performance estimation, but they are not adequate for dynamic control validation. Higher-fidelity dynamic models provide a more realistic description of the kite and tether dynamics, although at a higher computational cost [13, 14]. Therefore, the relevant gap is not only the availability of a dynamic kite model, but the lack of validation platforms in which the real control hardware, the real communication chain, and the real actuation system are tested in closed loop suitable for path-following studies.

This work presents a HIL that includes the physical actuators and communication hardware and applies it to the UC3M AWE prototype [7]. This distinction is important because the closed-loop performance depends not only on the control law, but also on communication delays, timing constraints, actuator dynamics, and implementation limits [8, 10]. These effects are difficult to assess in offline simulation alone, while flight tests are not always suitable for early-stage verification and debugging. In the proposed setup, a Ground Control Unit (GCU), wireless communications, and physical actuators operate in closed loop with a high-fidelity 3-lines kite dynamics simulation. The objective is not to replace flight testing, but to provide a repeatable validation stage to complement flight testing. The main contributions are threefold. Firstly, the module KiteElastic [14] of the open-source software LAKSA [15, 16], is integrated in a real-time environment compatible with the control architecture of the AWE machine. Secondly, the implementation of a closed-loop PHIL setup including the real GCU, wireless communications, CAN-based actuation, and the simulated plant. Thirdly, the operation of the platform in path-following conditions, with emphasis on the interaction between controller, communications, and actuation in real time is validated experimentally.

2 Methodology

The HIL setup comprises the same hardware elements used in the UC3M ground station [17]. Figure 1 shows the GCU and the physical actuators. It is a ground-actuated yo-yo machine where the lengths of the three tethers are varied by controlling the position of the actuators. The GCU is powered by a 48 V battery that supplies both the 48VDC for power the actuators and 24VDC for the logic of the GCU and the actuators through a DC-DC converter. Figure 2 shows the signal flow of the HIL architecture. On the left, the plant, namely the kite dynamics model and implemented in MATLAB/Simulink, generates the state variables that are encapsulated into the Micro Air Vehicle Link (MAVLink) messages. MAVLink is a communication protocol for bidirectional data exchange between Unmanned Aerial Systems and ground control stations [18]. The messages are transmitted through a Universal Asynchronous Receiver-Transmitter (UART) interface to the kite-side radio module. These messages are transmitted over a 2.4 GHz wireless link using ESP-NOW protocol [19] to the GCU, where they are unpacked and provided to the AWE system path controller. The controller computes the actuator commands, which are sent to the physical actuators through the CAN bus. The corresponding actuator information is then serialized and returned through UART to the Simulink environment, where it is decoded and applied to the plant model to close the loop. Dashed arrows denote physical communication links, whereas solid arrows indicate signal flow within each computational block.

The HIL platform was implemented on a standard laptop/PC to simulate plant, while the GCU, radio link, and actuation chain operated as physical hardware. Table 1 summarizes the hardware and software environment used in the experiments, together with the solver configuration and the main communication and control rates. These parameters define the timing constraints of the platform and determine the effective interaction between the simulated plant and the physical control hardware.

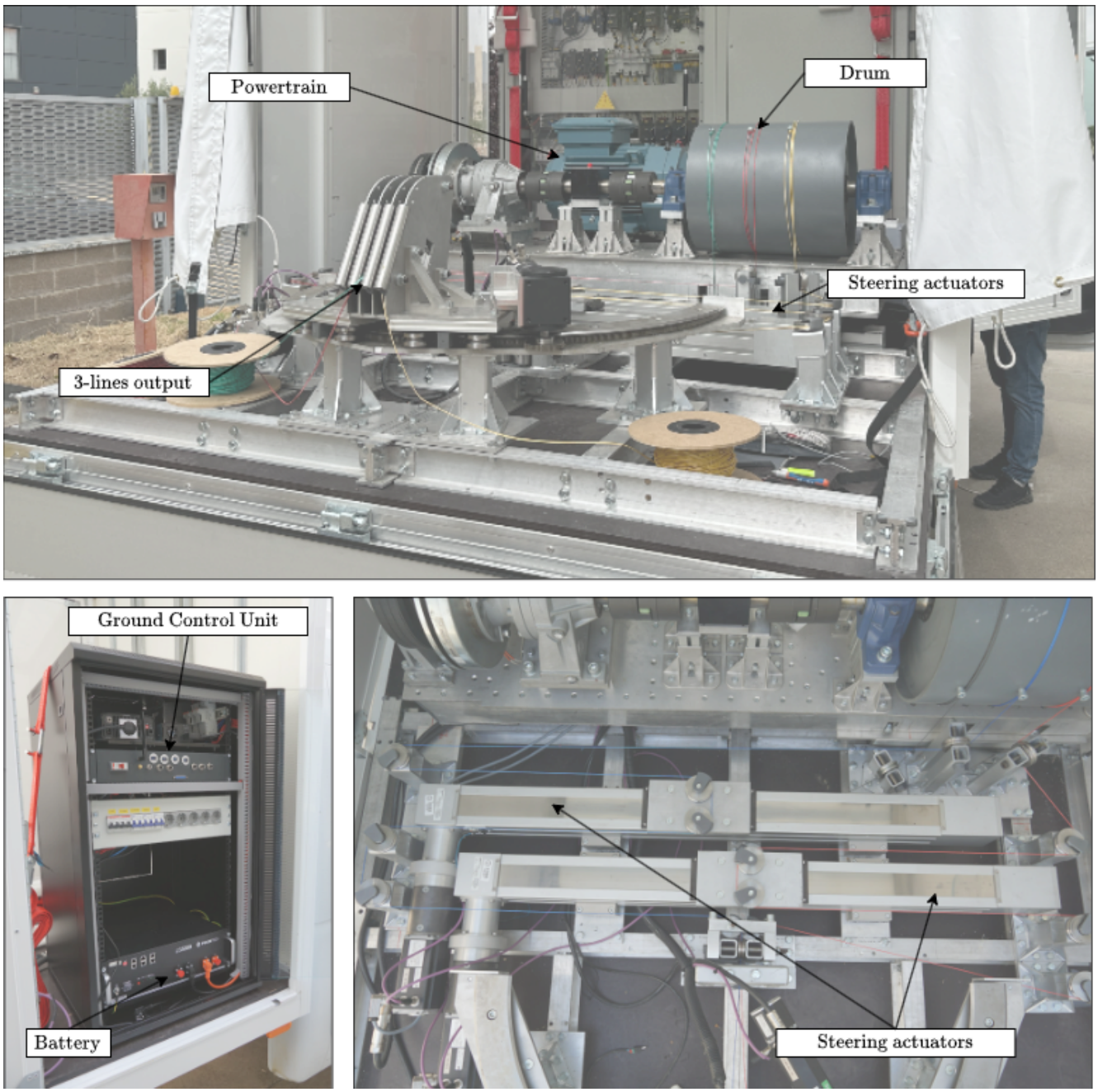

Fig. 1 Overview of the powertrain (top), electrical cabinet housing the Ground Control Unit and battery pack (left), and the physical actuators used for kite control (right).

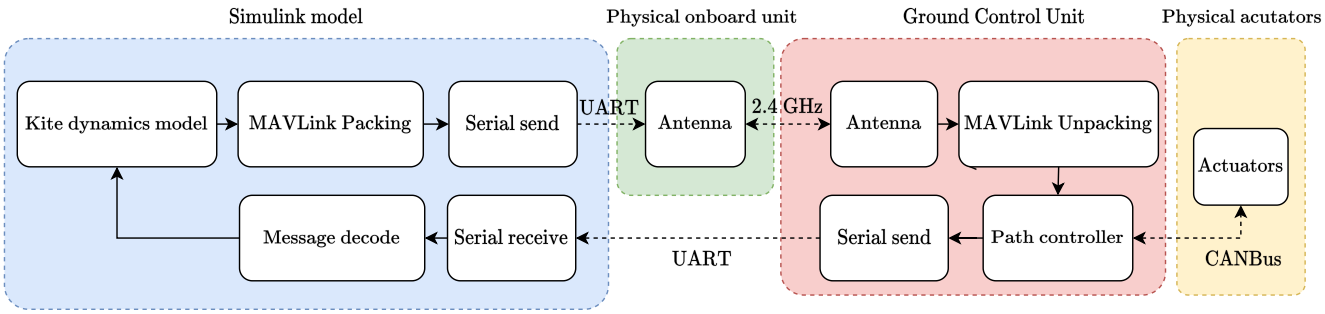

Fig. 2 Block diagram of the communication and control loop in the PHIL setup.

Table 1 Main implementation details of the HIL platform.

Item	Value	Item	Value
CPU	Intel i7-10750H @ 2.60GHz	Version	MATLAB R2025b
Execution mode	Rapid Accelerator (C)	Integrator	Runge-Kutta, fixed time step
Baudrate KCU	460800 bps	Baudrate GCU	500000 bps
MAVLink update rate	40 Hz	CAN bus rate	500000 bps
Radio link	2.4 GHz wireless link	Radio protocol	ESP-NOW
Controller frequency	40 Hz		

2.1 Kite dynamics model

The emulation system is built upon the open-source LAKSA KiteElastic simulator [14], which was ported to Simulink in a form compatible with C-code generation and integrated with the GCU of the UC3M AWE prototype [20]. The model accounts for tether flexibility and elasticity by representing each line as a set of lumped masses connected through spring–damper elements. The system is described in state-space form by

$$\frac{d\boldsymbol{x}_s}{dt} = f(\boldsymbol{x}_s; \boldsymbol{x}_c) \tag{1}$$

The flow F is not detailed in this work but the reader can find it in [14]. An inertial reference frame $\mathcal{S}_E$ is introduced with origin O_E at the tethers attachment points on the ground. The axes x_E and y_E lie on the flat ground plane, whereas the z_E axis points downward. A body-fixed reference frame $\mathcal{S}_B$ is also defined with origin at the kite center of mass, denoted by O_B. The axes x_B and z_B span the symmetry plane of the kite, with the x_B axis aligned with the spine.

The state vector $\boldsymbol{x}_s$ is defined as

$$\boldsymbol{x}_s = \begin{bmatrix} \boldsymbol{R}_K & \boldsymbol{v}_K & \boldsymbol{q}_K & \boldsymbol{\omega}_{BE} & \boldsymbol{R}_{P_{1,1}} & \dots & \boldsymbol{R}_{P_{3,10}} & \boldsymbol{v}_{P_{1,1}} & \dots & \boldsymbol{v}_{P_{3,10}} \end{bmatrix}^T \in \mathbb{R}^{193}, \tag{2}$$

where $\boldsymbol{R}_K$ is the kite position, $\boldsymbol{v}_K$ is the kite velocity, $\boldsymbol{q}_K$ denotes the kite attitude quaternion, and $\boldsymbol{\omega}_{BE}$ is the angular velocity of the body frame with respect to the Earth frame. The variables $\boldsymbol{R}_{P_{i,j}}$ and $\boldsymbol{v}_{P_{i,j}}$ denote the position and velocity of the tether particles, respectively.

The control vector $\boldsymbol{x}_c$ is defined as

$$\boldsymbol{x}_c = \begin{bmatrix} L_L & L_C & L_R \end{bmatrix}^T = \begin{bmatrix} L_{L,0} & L_{C,0} & L_{R,0} \end{bmatrix}^T + \frac{1}{2} \begin{bmatrix} -\Delta L_u & 0 & \Delta L_u \end{bmatrix}^T. \tag{3}$$

where L_L, L_C, and L_R denote the lengths of the left, center, and right tethers, respectively, and $L_{L,0}$, $L_{C,0}$, and $L_{R,0}$ are their initial values. The variable ΔL_u denotes the commanded actuator displacement.

Table 2 shows the parameters transmitted in real-time from the model. To emulate the behaviour of the Pixhawk 6C flight controller used on the physical kite [7], the Simulink model must transmit the same variables at the same rate as the onboard telemetry stream. Accordingly, it transmits the components of the state vector corresponding to the variables broadcast by the flight controller, namely $\boldsymbol{R}_K$, $\boldsymbol{v}_K$, $\boldsymbol{q}_K$, and $\boldsymbol{\omega}_{BE}$, at 40 Hz. A fixed-step fourth-order Runge–Kutta solver was used to integrate nummerically the equation 2.1 . The model was executed in Simulink Rapid Accelerator mode [21], which compiles the model into optimized C code to produce a standalone executable. By avoiding the Simulink interpreter at runtime, this configuration reduces computational cost and accelerates execution, which is particularly

advantageous for real-time simulation. The model parameters correspond to the FAZER XXL rigid-frame delta kite characterized in previous UC3M studies [22, 23]. Table 3 lists the parameters of the kite, thethers and bridle.

Table 2 MAVLink messages transmitted through the ESP32 bridge.

UART frame size [B]	Transmission period [ms]	Transmitted variables
40	25	$\boldsymbol{R}_K$, $\boldsymbol{v}_K$
44	25	$\boldsymbol{q}_K$, $\boldsymbol{\omega}_{BE}$
30	1000	Latitude, Longitude, Altitude

Table 3 Kite, tether, and bridle parameters.

Kite and tether parameters			
Description	**Symbol**	**Value**	**Units**
Kite chord	c	0.6	m
Kite span	b	3.66	m
Kite surface area	A	1.87	m^2
Kite mass	m	2.0	kg
Moment of inertia about x-axis	I_x	0.715	$kg\,m^2$
Moment of inertia about y-axis	I_y	0.115	$kg\,m^2$
Moment of inertia about z-axis	I_z	0.819	$kg\,m^2$
Product of inertia	I_{xz}	0	$kg\,m^2$
Tether radius	r_t	1	mm
Tether linear density	μ	0.0018	kg/m
Tether Young's modulus	E	180	GPa
Tether damping coefficient	c_t	350	N s/m
Tether drag coefficient	$C_{D,t}$	1.1	–
Nominal tether length	L_0	100	m
Central tether length	L_C	100.535	m

Bridle connection points				
Point	**x_B (m)**	**y_B (m)**	**z_B (m)**	**Bridle length (m)**
1	-0.083	0	0.015	1.219
2	-0.083	0	0.015	1.219
3	-0.083	1.38	0.015	1.170
4	-0.083	-1.38	0.015	1.170
5	0.406	0.45	0.015	0.731
6	0.406	-0.45	0.015	0.731
7	0.100	0.93	0.015	1.073
8	0.100	-0.93	0.015	1.073

2.2 Path control

The control strategy follows the hybrid guidance-and-control architecture initially described in [24] and later adapted to the UC3M three-line rigid-framed kite in [7]. In summary, the position and heading angle of the kite on the wind sphere are determined by three angles, that is, λ for the elevation, δ for the

azimuth, and ψ for the heading. These values, as estimated by the flight computer during flight tests or by the Simulink model for the HIL setup, are then fed into the guidance module, which then provides a setpoint of the heading angle (ψ_{sp}).

The desired figure-eight flight path is divided into two straight segments and two turning sections, as shown in 3 b). During the straight segments, the guidance module computes ψ_{sp} such as the kite points towards the attractor waypoints $R^{\pm}$. During turns, ψ_{sp} is defined such as the kite is orientated perpendicular to the vector $\overline{C_{\pm}O_K}$ and pointing in the up-turning direction. The switching logic is implemented by a finite-state machine (FSM), whose transitions are triggered by azimuth thresholds $\delta_{L^{\pm}}$ and heading thresholds $\psi_{L^{\pm}}$ respectively.

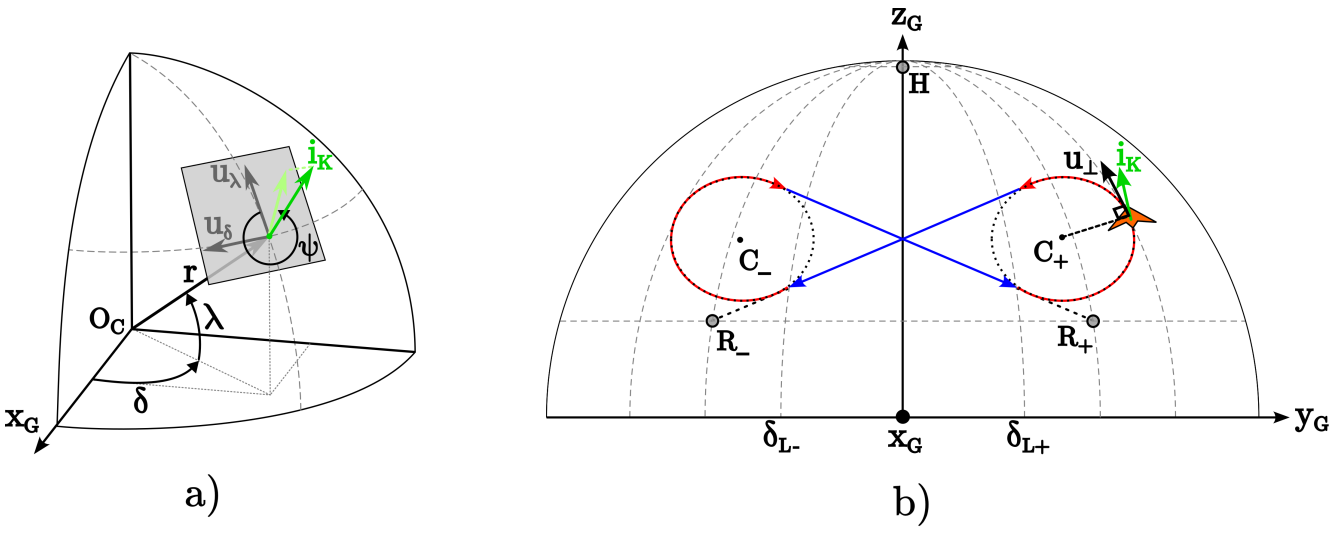

Fig. 3 Control variables used in the path-following strategy. (a) Definition of azimuth, elevation, and heading angles. (b) Turn centers C_- and C_+, and attractor points R_- and R_+ used by the hybrid guidance law [7]

A discrete Proportional-Integral-Derivative (PID) controller tracks the heading reference and generates the commanded left–right line-length difference ΔL_u. This variable is then converted, through the pulley kinematics, into individual motor-angle set-points for the actuator drives. Each actuator features a built-in cascade position controller, that is, a position PID with speed and acceleration feed-forward, followed by a current PI loop, both including anti-windup protection. The controller runs at 40 Hz and preserves the same implementation used in the experimental ground station. This is important because the objective of the platform is not only to evaluate the guidance law in simulation, but also to validate the complete embedded control chain under realistic communication and actuation conditions. The tuning parameters ($R^{\pm}$, $C^{\pm}$, $\delta_{L^{\pm}}$, $\psi_{L^{\pm}}$, as well as the PID's gains) provide direct control over the lateral amplitude, average elevation, and turn radius of the figure-eight trajectory. A detailed description of the guidance and control algorithms can be found in Ref. [7].

3 Results

This section presents the results obtained with the proposed HIL platform at two different levels. First, Sections 3.1 and 3.2 assess the performance of specific blocks of the platform separately, namely the real-time computational capability of the simulator and the latency introduced by the communication and actuation chain. Then, Section 3.3 evaluates the complete closed-loop operation of the HIL setup in a representative path-following experiment, in which the simulated nonlinear plant, the communication interfaces, the GCU, and the physical actuators operate together to reproduce a figure-eight flight trajectory.

3.1 Performance of the real-time model

The results in Fig. 4 and Table 4 are reported as a function of the fixed integration step, Δt, with a simulated time of 20 s. The real-time factor (RTF) is defined as the ratio between the simulated time and the computation-only execution time, and therefore indicates the real-time capability of the model, with values above one corresponding to faster-than-real-time execution. The average task execution time, $\mathrm{TET}_{\mathrm{avg}}$, is computed as the average computation time required to resolve one simulation step. The average CPU load is estimated as the ratio between $\mathrm{TET}_{\mathrm{avg}}$ and Δt, expressed as a percentage, so that values below 100% indicate that the simulation is computationally capable of real-time operation. The wall-clock time denotes the total elapsed execution time measured externally, including initialization and compilation overheads, whereas the pure execution time corresponds only to the time effectively spent in numerical computation during the simulation. To achieve the real-time capability with this setup, the minimum time-step to avoid overrun errors is $\Delta t = 2 \cdot 10^{-4}$s.

Table 4 Computational performance metrics for different fixed integration steps.

Δt (s)	RTF	$\mathrm{TET}_{\mathrm{avg}}$ (ms)	CPU load (%)	Wall-clock (s)	Pure exec. (s)
1.0×10^{-3}	4.27	0.234	23.42	28.66	4.68
5.0×10^{-4}	2.48	0.202	40.33	33.02	8.07
2.0×10^{-4}	1.23	0.162	81.06	40.65	16.21
1.0×10^{-4}	0.58	0.171	171.08	59.56	34.22

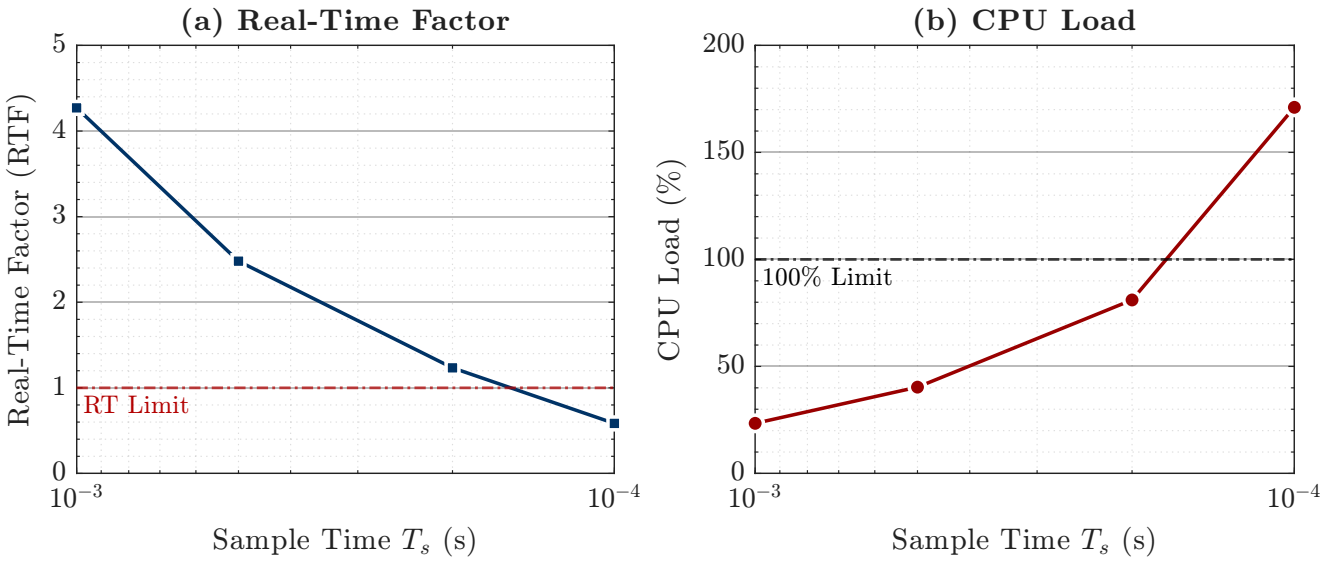

Fig. 4 a) Real-Time Factor in the Simulation b) CPU load where 100% is the maximum capacity of the device

3.2 Communication latency

A quantitative characterization of communication latency is required to assess the real-time capability of the proposed control architecture, understood as the time delay introduced by each stage of the control chain from the position and attitude data being sent from the Simulink model to the actuator feedback coming back from the GCU. Since the closed loop involves multiple hardware devices and several communication interfaces, the total delay is the cumulative effect of all transmission and processing stages. For this reason, the latency of the complete communication chain is evaluated in the following results.Table 5 summarizes the delays in the communication. The MAVLink burst is transmitted from the plant to the GCU through a UART/ESP-NOW/UART bridge. Under the considered configuration,

the complete burst is available at the GCU after approximately 6.55 ms. The GCU then communicates with left and right actuators through CANopen at 500 kbps. In the implemented driver, each position command is transmitted through three consecutive CAN frames using Process Data Objects (PDO): one 8-byte PDO containing the target position and velocity, followed by two 2-byte control-word frames. A software delay of 500 μs is inserted between consecutive transmissions. Actuator feedback is obtained through a remote PDO request followed by one 8-byte response frame containing position and velocity. For the two actuators addressed sequentially, the resulting CAN communication delay is approximately 3.58 ms at bus level, or 4.58 ms when the software waiting times inserted by the GCU are included. Therefore, the complete end-to-end delay from the start of MAVLink transmission at the plant to command delivery and position reception for both actuators is approximately 11.1 ms including software delays, excluding the internal actuator response time.W ith $\approx$ 11.13 ms of communication delay, the frequency of the microcontroller cannot be greater than 75 – 80Hz. With the actual setup, the delay allows a frequency of f = 40Hz in the controller with a safety margin.

Table 5 Summary of communication stages and associated delays.

Stage	Communication type	Delay [ms]
Plant (PC) → onboard ESP32	UART (460800 bps)	2.691
Onboard ESP32 → Ground ESP32	ESP-NOW	1.336
Ground ESP32 → GCU	UART (500000 bps)	2.480
Plant → GCU subtotal	**UART + ESP-NOW + UART**	**6.547**
Command to right actuator	CANopen/CAN	1.474
Feedback from right actuator	CANopen/CAN	0.316
Command to left actuator	CANopen/CAN	1.474
Feedback from left actuator	CANopen/CAN	0.316
GCU ↔ actuators subtotal	**CANopen/CAN**	**3.580**
GCU software waiting times	Forced delays	1.000
End-to-end total	**All links**	**11.127**

3.3 Path controller

Once the real-time capability of the simulator and the communication latency of the platform have been characterized separately, the complete HIL setup is evaluated in a representative closed-loop path-following experiment. In this test, the plant, the wireless communication chain, the GCU, and the physical actuators are operated together using the implementation settings described in Section 2 in order to assess the tracking of a figure-eight reference trajectory. Figure 5 shows a representative three-dimensional trajectory obtained with the proposed setup. During the complete experiment, the loop between the simulated plant, the communication interfaces, the GCU, and the physical actuators remained closed and stable. Figure 6 shows the heading reference, ψ_{ref}, together with the measured heading response, ψ. The controller follows the commanded signal consistently during the complete maneuver, and the transitions between straight-flight and turning phases are completed without loss of closed-loop stability. The measured response remains close to the reference and reproduces the sequence of heading reversals required to generate the figure-eight trajectory shown in Fig. 5. These results indicate that the proposed HIL platform is suitable for validating the interaction between the path-following controller and the nonlinear plant under representative operating conditions.

Figure 7 presents the actuator command ΔL_u together with the state of the finite-state machine (FSM). The sequence of controller states is consistent with the expected alternation between straight segments and turning maneuvers. In addition, the actuator command remains bounded throughout the experiment,

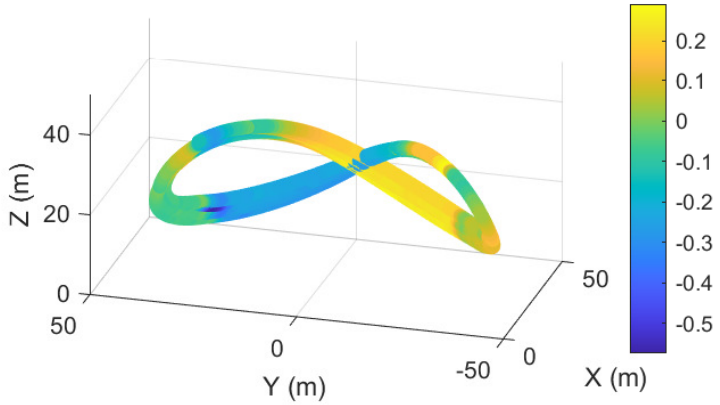

Fig. 5 Three-dimensional kite trajectory obtained in the closed-loop HIL experiment. The color bar represents the commanded differential line length ΔL_u.

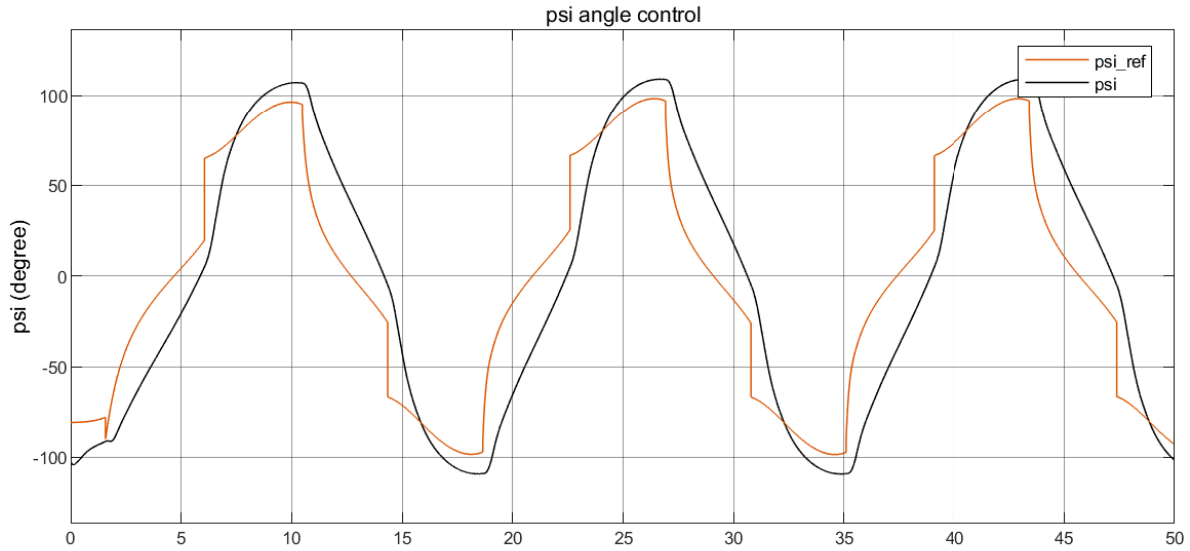

Fig. 6 Commanded heading ψ_{ref} and measured heading ψ during a representative closed-loop experiment.

which confirms that the complete chain composed of guidance law, heading controller, communications, and physical actuation behaves coherently when coupled to the simulated kite model.

4 Conclusions

This work has presented a hardware-in-the-loop platform for the closed-loop validation of an AWE path controller under representative implementation conditions. The results demonstrate that the proposed setup constitutes a suitable intermediate validation stage between offline simulation and field experiments. From the computational point of view, the real-time simulator based on the LAKSA KiteElastic model was successfully integrated into a Simulink environment and achieved real-time performance for fixed integration steps down to 2×10^{-4} s. From the communications perspective, the latency analysis showed that the complete transmission and actuation chain introduces an end-to-end delay of approximately 11.1 ms, which is compatible with the implemented controller frequency of 40 Hz and provides sufficient margin for stable operation. Finally, the closed-loop path-following experiments confirmed that the controller is able to track the commanded heading reference and generate stable figure-eight trajectories

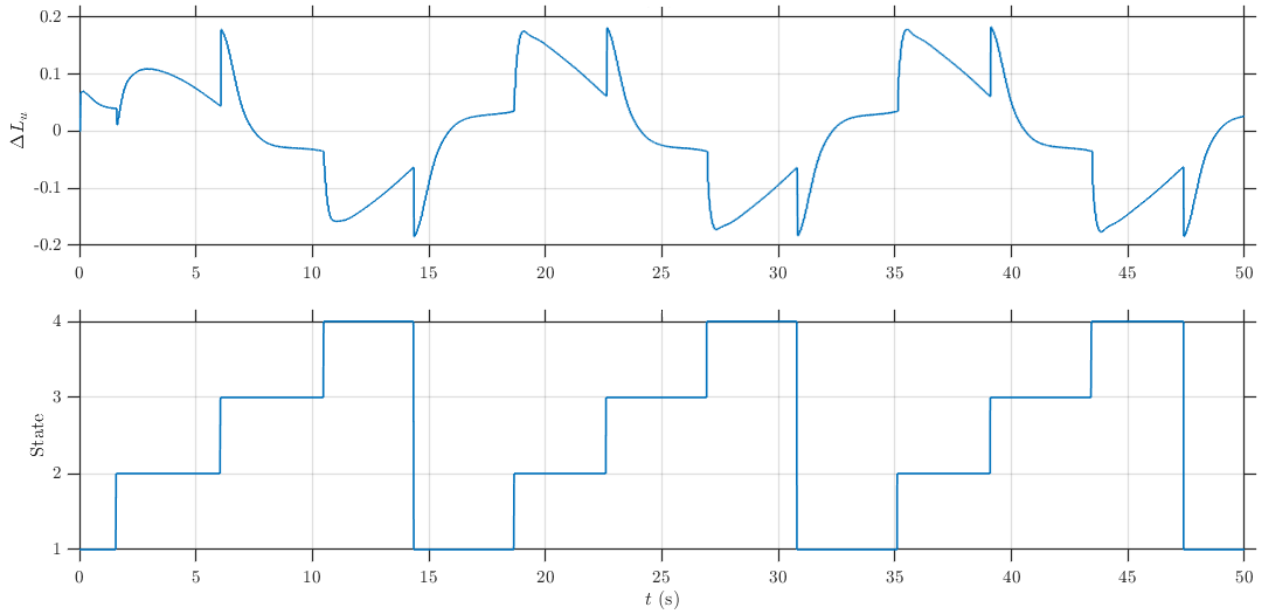

Fig. 7 Actuator command ΔL_u and finite-state machine (FSM) state during the closed-loop HIL experiment.

while preserving coherent interaction between the simulated nonlinear plant, the real GCU, the wireless communication link, and the physical actuators.

Overall, the proposed HIL setup provides a framework to assess not only the guidance and control strategy, but also the effects of communication delays, actuator dynamics, and embedded implementation constraints prior to flight testing. In this way, the platform contributes to reducing experimental risk, accelerating controller development, and improving confidence in the integrated system before on-field deployment. Future work will extend the present HIL architecture by incorporating the mechanical-to-electrical power conversion stage of the ground station, together with an electric machine that emulates the torque generated by the kite. This extension will make it possible to reproduce not only the flight-control loop, but also the coupling between the airborne subsystem and the power-generation stage, thus moving towards a more comprehensive experimental environment for the validation of complete AWE systems.

Acknowledgments

This work has been supported by the research project PID2022-141520OB-I00 funded by MICIU/AEI/10.13039/501100011033 and FEDER, UE. Work by F. DeLosRíos-Navarrete was supported by the grant with reference IND2022/AMB-23521 funded by Comunidad de Madrid.

Declaration of Use of Artificial Intelligence

Artificial intelligence was not used in the work presented.

References

[1] Miles L. Loyd. Lawrence livermore national laboratory, livermore, calif. *J. Energy*, 1980.

[2] Antonello Cherubini, Andrea Papini, Rocco Vertechy, and Marco Fontana. Airborne wind energy systems: A review of the technologies. *Renewable and Sustainable Energy Reviews*, 51:1461–1476, 2015. doi: 10.1016/j.rser.2015.07.053.

[3] Chris Vermillion, Mitchell Cobb, Lorenzo Fagiano, Rachel Leuthold, Moritz Diehl, Roy S. Smith, Tony A. Wood, Sebastian Rapp, Roland Schmehl, David Olinger, and Michael Demetriou. Electricity in the air: Insights from two decades of advanced control research and experimental flight testing of airborne wind energy systems. *Annual Reviews in Control*, 52:330–357, 2021. doi: 10.1016/j.arcontrol.2021.03.002.

[4] Alexander Bormann, Maximilian Ranneberg, Peter Kövesdi, Christian Gebhardt, and Stefan Skutnik. *Development of a Three-Line Ground-Actuated Airborne Wind Energy Converter*, pages 427–436. Springer Berlin Heidelberg, Berlin, Heidelberg, 2013. ISBN: 978-3-642-39965-7. doi: 10.1007/978-3-642-39965-7$_2$4.

[5] Rolf van der Vlugt, Johannes Peschel, and Roland Schmehl. *Design and Experimental Characterization of a Pumping Kite Power System*, pages 403–425. Springer Berlin Heidelberg, Berlin, Heidelberg, 2013. ISBN: 978-3-642-39965-7. doi: 10.1007/978-3-642-39965-7$_2$3.

[6] Lorenzo Fagiano, Aldo U. Zgraggen, Manfred Morari, and Mustafa Khammash. Automatic crosswind flight of tethered wings for airborne wind energy: Modeling, control design, and experimental results. *IEEE Transactions on Control Systems Technology*, 22(4):1433–1447, 2014. doi: 10.1109/TCST.2013.2279592.

[7] Francisco DeLosRíos-Navarrete, Jorge González-García, Iván Castro-Fernández, and Gonzalo Sánchez-Arriaga. A small-scale and autonomous testbed for three-line delta kites applied to airborne wind energy. *Wind Energy Science*, 10(6):1153–1166, 2025. doi: 10.5194/wes-10-1153-2025.

[8] Florian Bauer, Christoph M. Hackl, Keyue Smedley, and Ralph M. Kennel. "Virtual"-Power-Hardware-in-the-Loop Simulations for Crosswind Kite Power with Ground Generation. In *2016 American Control Conference (ACC)*, pages 4071–4076, Boston, MA, USA, 2016. IEEE. doi: 10.1109/ACC.2016.7525561.

[9] Roystan Vijay Castelino, Pankaj Kumar, Yashwant Kashyap, Anabalagan Karthikeyan, Manjunatha Sharma K., Debabrata Karmakar, and Panagiotis Kosmopoulos. Exploring the potential of kite-based wind power generation: An emulation-based approach. *Energies*, 16(13):5213, 2023. doi: 10.3390/en16135213.

[10] Pankaj Kumar, Yashwant Kashyap, Roystan Vijay Castelino, Anabalagan Karthikeyan, Manjunatha Sharma K., Debabrata Karmakar, and Panagiotis Kosmopoulos. Laboratory-scale airborne wind energy conversion emulator using OPAL-RT real-time simulator. *Energies*, 16(19):6804, 2023. doi: 10.3390/en16196804.

[11] C. Nicolás-Martín, D. Santos-Martín, F. DeLosRíos-Navarrete, and J. González-García. Airborne wind energy system test bench electrical emulator. *Wind Energy Science Discussions*, 2025:1–23, 2025. doi: 10.5194/wes-2025-19.

[12] Rolf van der Vlugt, Anna Bley, Michael Noom, and Roland Schmehl. Quasi-steady model of a pumping kite power system. *Renewable Energy*, 131:83–99, 2019. doi: 10.1016/j.renene.2018.07.023.

[13] S. G. C. De Groot, J. Breukels, R. Schmehl, and W. J. Ockels. Modelling kite flight dynamics using a multibody reduction approach. *Journal of Guidance, Control, and Dynamics*, 34(6):1671–1682, 2011. doi: 10.2514/1.52686.

[14] Gonzalo Sánchez-Arriaga, Jose Antonio Serrano-Iglesias, Rachel Leuthold, and Moritz Diehl. Modeling and natural mode analysis of tethered multi-aircraft systems. *Journal of Guidance, Control, and Dynamics*, 44(6):1199–1210, 2021. doi: 10.2514/1.G005075.

[15] G. Sánchez-Arriaga, A. Pastor-Rodríguez, M. Sanjurjo-Rivo, and R. Schmehl. A lagrangian flight simulator for airborne wind energy systems. *Applied Mathematical Modelling*, 69:665–684, May 2019. ISSN: 0307904X. 20 citations (Crossref) [2025-06-04]. doi: 10.1016/j.apm.2018.12.016.

[16] G. Sánchez-Arriaga, A. Pastor-Rodríguez, R. Borobia-Moreno, and R. Schmehl. A constraint-free flight simulator package for airborne wind energy systems. *Journal of Physics: Conference Series*, 1037:062018, June 2018. ISSN: 1742-6588, 1742-6596. 4 citations (Crossref) [2025-06-04]. doi: 10.1088/1742-6596/1037/6/062018.

[17] Francisco DeLosRıos-Navarretea, Jorge González-Garcıab, Carolina Nicolás-Martınc, David Santos-Martınc, and Gonzalo Sánchez-Arriagab. Testing of a ground-controlled airborne wind energy system prototype. 2025.

[18] MAVLink Guide. `https://mavlink.io/`.

[19] Espressif Systems. ESP-NOW, 2026. ESP-IDF Programming Guide, ESP32, stable documentation. `https://docs.espressif.com/projects/esp-idf/en/stable/esp32/api-reference/network/esp_now.html`.

[20] Francisco DeLosRíos-Navarrete, Jorge González-García, Carolina Nicolás Martín, David Santos-Martin, and Gonzalo Sanchez-Arriaga. Testing of a ground-controlled airborne wind energy system prototype. In *Wind Energy Science Conference (WESC 2025)*, Nantes, France, 2025. Oral presentation. doi: 10.13140/RG.2.2.33706.73926, `https://www.researchgate.net/publication/393460902`.

[21] Guy Rouleau. Speed up your simulations with rapid accelerator mode, 2023. `https://www.mathworks.com/company/technical-articles/speed-up-your-simulations-with-rapid-accelerator-mode.html`.

[22] Iván Castro-Fernández, Ricardo Borobia-Moreno, Rauno Cavallaro, and Gonzalo Sánchez-Arriaga. Three-dimensional unsteady aerodynamic analysis of a rigid-framed delta kite applied to airborne wind energy. *Energies*, 14(23):8080, 2021. doi: 10.3390/en14238080.

[23] I. Castro-Fernández, R. Cavallaro, R. Schmehl, and G. Sánchez-Arriaga. Unsteady aerodynamics of delta kites for airborne wind energy under dynamic stall conditions. *Wind Energy*, 27(9):936–952, 2024. doi: 10.1002/we.2932.

[24] Uwe Fechner. *A Methodology for the Design of Kite-Power Control Systems*. PhD thesis, Delft University of Technology, 2016. doi: 10.4233/85efaf4c-9dce-4111-bc91-7171b9da4b77.